Article

Cellulose Acetate Supported MOF-5/Crystalline Nanocellulose Composite Film as an Adsorbent Material for Methylene Blue Removal from Aqueous Solutions
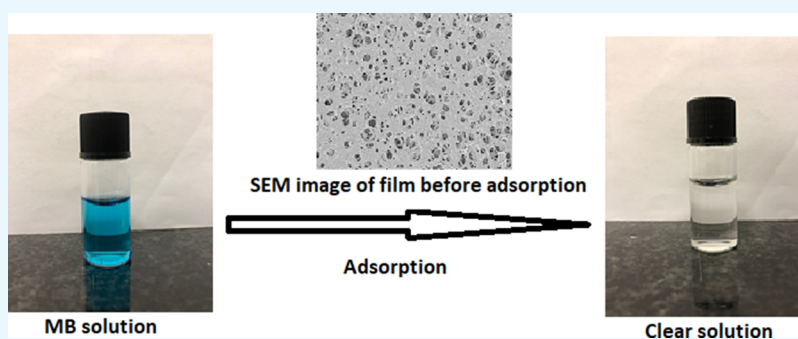
Lebogang Manamela and Nolwazi Nombona*

Read Online

ACCESS | Metrics & More | Article Recommendations

ABSTRACT: In this study, a novel, low-cost, and efficient adsorbent film was fabricated by a solvothermal method. The adsorbent film was developed to be hydrolytically stable, not vulnerable to aggregation in aqueous environments, and not prone to secondary contamination. The adsorbent consists of cellulose acetate (CA) as a support embedded with a MOF-5/crystalline nanocellulose (CNC) composite material. The CA-supported MOF-5/CNC film was characterized using a variety of techniques, including X-ray diffraction, thermal gravimetric analysis, scanning electron microscopy, X-ray photoelectron spectroscopy, and Fourier transform infrared spectroscopy, which revealed hydroxyl and carbonyl functional groups on the adsorbent film. The film was evaluated for the adsorptive removal of methylene blue (MB) from an aqueous solution. Adsorption was characterized by a rapid increase in MB adsorption during the first hour with equilibrium achieved within 4−5 h into the adsorption process. The maximum adsorption capacity was determined to be 4.29 mg/g and the maximum dye removal efficiency was 77%. The MB adsorption process best fitted the Freundlich isotherm and pseudo-second-order kinetic models. Thermodynamic studies showed that the adsorption was exothermic and feasible. The adsorbent film showed admirable regeneration ability, demonstrating its cost-effectiveness and its potential as a promising material for wastewater treatment.

INTRODUCTION

The textile industry has been listed as one of the emerging contributors of CO_2 emissions and, unfortunately, the textile sector is also among the largest contributors of wastewater with an annual worldwide dyestuff production of over 7×10^5 tons.[1,2] One of the ways in which dye effluents enter waterbodies such as rivers and lakes is due to the inability of dye mixtures to completely attach to intended textiles.[3] Synthetic dyes are toxic by nature,[4] stable,[5] and pose a risk to the environment and human health.[6,7]

The removal of organic dyes from aquatic systems is crucial in eliminating harmful effects from reduced sunlight penetration caused by dye pollution, which often leads to a decrease in photosynthesis. Methylene blue (MB) is frequently used in the textile industry to print cotton and dye leather. Several dye removal techniques have been reported and these include membrane separation,[8] coagulation/flocculation,[9] and ozona-

tion.[10] The most preferred method among these has been physical adsorption using solid materials, as it is highly efficient in the removal and treatment of contaminants in wastewater.[11−13] This low-cost technology is a separation process that concentrates molecules (contaminants) on the surface of a solid adsorbent.[14] Various materials have been employed as adsorbents with activated carbon being the most common commercial adsorbent.[15−17] Despite being the most established adsorbent, activated carbon is expensive and has high

reactivation costs, and this suggests the need for cheaper, efficient, and reusable adsorbents.[18−21]

Metal−organic frameworks (MOFs) are reported to play an important role in the adsorption of organic pollutants due to their high surface area, high porosity, and biocompatibility.[22−24] Zr-based MOFs have been reported to have high adsorption capacities for the removal of organic dyes.[12,25−27] These MOFs are stable in aqueous media and can withstand harsh chemical environments, moisture and temperature changes.[28] However, their high cost of synthesis makes them uneconomical as adsorbents for organic dye removal; as a result, there is a need for cheaper MOF alternatives. One of the major challenges that cheaper MOFs encounter when applied in water remediation technologies is poor hydrolytic stability.[29] To increase water stability, high oxidation metals have been incorporated in the MOF structure with linker groups such as pyrazole to increase the metal-linker bonding strength.[30] Coating of the MOFs' internal or external surface with hydrophobic materials has also been shown to increase hydrolytic stability.[31] It was previously demonstrated that the external surface hydrophobization of MOFs has the potential to lower surface area and enhance water stability.[32] Ding et al. developed a polymerization approach to coat the surface of HKUST-1, ZIF-67, and MIL-125 with 2,2,2-trifluoroethyl methacrylate and 3-methacryloxypropyltrimethoxysilane to synthesize water-stable MOF composites without significant change of their pore features.[33] The incorporation of styrene to MOFs has been shown to improve the hydrolytic stability of MOFs, and their performance[34] hence, it is important to fabricate a MOF-based material with hydrolytic stability without compromising functionality. While these modifications improve hydrolytic stability, they do not address potential aggregation, which might minimize surface area for adsorption and cause secondary contamination. To manage these challenges, MOFs have been embedded in membrane support materials,[22,35−37] and they have been incorporated in the matrix of polymeric materials.[38] This approach was found to address secondary contamination; however, MOF particles could still aggregate on the membrane support.[22,37] Aggregation on polymer membrane supports occurs due to the attraction of MOF particles to one another coupled with poor MOF adhesion to most polymers. Duan et al. reported MOF aggregation on polymeric membrane surfaces when using an adsorption-filtration technique for MOF immobilization, resulting in secondary contamination.[22]

This study explores the use of MOF-5 as an adsorbent material for the removal of MB from aqueous solutions. MB was selected as a model contaminant, as it is frequently used in the textile industry and is an abundant pollutant in the aquatic system. Its cationic nature enables it to interact and penetrate the negatively charged cellular membranes of marine animals and human beings and this can lead to bioaccumulation of MB, which can cause illnesses such as cancer.[39] In this work, MOF-5 was used as an active material for the adsorptive removal of MB from water due to its relatively high surface area, which provides active sites for adsorption, it is cheaper compared to most MOFs, can be used multiple times for adsorption, and can be tailored to have high affinity for cationic dyes. The drawbacks of using MOFs for water remediation are that they have low water stability, they aggregate in aqueous solution, are sensitive to acidic/alkaline environments, and are hard to recycle. The functionalization of MOFs with various materials has been shown to overcome some of these challenges. To

maximize the strength of the adsorbent, crystalline nanocellulose (CNC) was combined with MOF-5 to form a powdered-crystalline composite (MOF-5/CNC) for improved hydrolytic stability. The MOF-5/CNC was embedded in a cellulose acetate (CA) matrix to form an adsorbent film (CA-supported MOF-5/CNC) to avoid secondary contamination when it was applied for the adsorptive removal of MB from water. The multi-component film also acts to eliminate aggregation suffered by MOFs and renders the film recyclable. The impact of initial concentration, pH, contact time, and temperature on the adsorption process was examined. The adsorption isotherms and adsorption kinetics were evaluated by using models.

■ EXPERIMENTAL SECTION

Materials. Acetone (99.9%), *N,N*-dimethylformamide (DMF, 99.9%), chloroform (CH$_3$Cl, 99%), and sulfuric acid (H$_2$SO$_4$, 98%) were purchased from Radchem. Zinc nitrate hexahydrate (Zn(NO$_3$)$_2$·6H$_2$O, 98%), microcrystalline cellulose (MCC, 11 wt %), CA (39.3−40.3%), MB (98%), and terephthalic acid (BDC, 99%) were purchased from Sigma-Aldrich.

Synthesis of a CA-Supported MOF-5/CNC Adsorbent Film. Pristine MOF-5 was prepared following a reported method.[40] Briefly, 6.5 g of zinc nitrate hexahydrate and 1.2 g of BDC were dissolved in 180 mL of DMF, and the mixture was stirred for 30 min. Thereafter, the mixture was heated in an oven at 105 °C for 24 h. After being cooled to room temperature, the white powder was washed with DMF and repeatedly washed with chloroform. The product, MOF-5, was vacuum-dried at 60 °C for 12 h.

CNC was synthesized using a reported procedure.[41] MCC (1 g) was added to 30% H$_2$SO$_4$ under vigorous stirring for 1 h. Distilled iced water was used to quench the mixture, and the solution was sonicated for 10 min followed by centrifugation for 30 min. The aqueous supernatant was discarded, and fresh distilled water was added to the pellet, followed by ultrasonication before further centrifugation. This washing process was repeated until the pH of the supernatant was neutral. The resulting pellet was freeze-dried to yield powder CNC.

14.7 wt % MOF-5/CNC was synthesized by adding 1.2 g of BDC to 90 mL of DMF. The mixture was stirred for 10 min, and CNC (50 mg) was added to the reaction mixture. In a separate reaction vessel, 5 g of Zn(NO$_3$)$_2$·6H$_2$O was added to 90 mL of DMF. The mixtures were stirred separately for 15 min, followed by ultrasonication for 15 min. The mixtures were combined, and the resulting mixture was stirred for 15 min, followed by ultrasonication for 15 min and heating at 50 °C under vigorous stirring for 2 h. The solution was cooled to room temperature and centrifuged to isolate the solid material. The product was washed with DMF and vacuum-dried at 60 °C for 6 h to yield MOF-5/CNC.

The synthesized MOF-5/CNC composite was supported on CA by dissolving 7.5 g of CA in 76 mL of DMF followed by stirring for 18 h at room temperature.[42] The solution was degassed with nitrogen at room temperature overnight. In a separate reaction vessel, MOF-5/CNC in DMF was stirred and sonicated for 10 min. Thereafter, 3.3 mL of CA solution was added to the reaction vessel, and the resulting mixture was stirred vigorously for 1 h, followed by sonication for 30 min to obtain a viscous gel. The gel was drop-cast on a glass slide until a thickness of 0.2 mm was obtained. The coated glass slide was placed in a water bath at 6 °C for 4 h. The coated glass slide

was removed from the water bath, and another glass slide was placed on top of the newly formed mat; subsequently, a force of 50 N was exerted on the film for 30 min. The film was air-dried overnight.

Adsorption Experiments. Solutions of MB (1−6 mg/L) were prepared from a 400 mg/L stock solution. The adsorbent mats (7 mm × 15 mm) were immersed in 3 mL of MB solutions and agitated in a bath shaker for 6 h. The adsorption behavior of the material at different parameters, such as contact time, solution pH, temperature, and initial MB concentration, was investigated. The percentage of MB removal was calculated using eq 1 and adsorption capacity, q_e, was calculated using eq 2:

$$\%\text{MB removal} = \frac{C_i - C_e}{C_i} \times 100\% \tag{1}$$

$$q_e = \frac{C_i - C_e}{m} \times V \tag{2}$$

where C_i is the initial concentration of MB solution (mg/L), C_e is the equilibrium concentration of MB solution (mg/L), q_e is the equilibrium adsorption capacity (mg/g), V is the volume of the solution (mL), and m is the mass of the adsorbent (g).

To assess the reusability of the film, recyclability tests were performed. The adsorbent film was removed from the MB solution after an adsorption cycle and immersed in methanol to desorb the dye. The desorption solvent (methanol) was shaken for 4 h, and the film was removed to air-dry for 1 h, ready for the next adsorption cycle.

Adsorption Isotherms. Adsorption isotherms were used to establish the effectiveness of the adsorption process and assess the affinity of the adsorbent for the adsorbates, thus describing the interactions between the adsorbent and the adsorbates. In this study, the adsorbents were analyzed using Langmuir and Freundlich isotherms. The Langmuir isotherm operates under the assumption that the adsorption process is monolayer adsorption and occurs on a homogeneous surface while the Freundlich isotherm assumes the adsorption process is multilayer and occurs on a heterogeneous surface. Equations 3 and 4 show the linearized Langmuir and Freundlich adsorption isotherm models, respectively:

$$\frac{1}{q_e} = \frac{1}{K_L q_{max}} \times \frac{1}{C_e} + \frac{1}{q_{max}} \tag{3}$$

$$\log(q_e) = \log(K_F) + \left(\frac{1}{n}\right)\log(C_e) \tag{4}$$

From the equations, q_{max} is the maximum adsorption capacity of the adsorbent (mg/g), and K_L is the Langmuir constant, which is related to adsorption affinity. The larger the values of K_L, the stronger the interactions between the adsorbent and adsorbate. K_F is the Freundlich isotherm constant. The gradient of the linear form of the equation, $1/n$, is a function of the strength of the adsorption process. The normal adsorption process occurs when $\frac{1}{n} > 1$. When $\frac{1}{n} > 1$, cooperative adsorption is taking place. R_L is a separation factor and is calculated using eq 5 below:

$$R_L = \frac{1}{1 + K_L C_i} \tag{5}$$

where K_L is the Langmuir constant and C_i is the initial adsorbate concentration. The adsorption nature is not favored

when $R_L > 1$, linear when $R_L = 1$, favorable when $0 < R_L < 1$, and irreversible when $R_L = 0$.

Adsorption Kinetics. Adsorption kinetics provide a platform to understand the adsorption mechanisms, such as mass transfer and chemical reactions during adsorption. In this study, the kinetic data obtained was analyzed by pseudo-first-order and pseudo-second-order models, using eqs 6 and 7, respectively:

$$\ln(q_e - q_t) = \ln(q_e) - k_1 t \tag{6}$$

$$\frac{1}{q_t} = \frac{1}{K_2 q_e^2} + \frac{1}{q_e}t \tag{7}$$

where q_e is the adsorption capacity at equilibrium, q_t (mg/g) is the adsorption capacity at time t, t (minutes) is the contact time, k_1 is the first-order equilibrium constant, and k_2 is the second-order equilibrium constant. The diffusion mechanisms of the adsorption process were studied using the intraparticle diffusion rate equation, eq 8:

$$q_t = k_{id} t^{1/2} + I \tag{8}$$

where k_{id} is the intraparticle diffusion rate constant (mg/g·min$^{-1/2}$) and I is the thickness of the boundary layer. The Bangham diffusion model was studied to understand the adsorption mechanism using eq 9:

$$\log\log\left(\frac{C_i}{C_i - q_t}\right) = \log\left(\frac{k_b m}{2.303 V}\right) + \alpha \log\left(t\right) \tag{9}$$

where k_b and α are constants. The pore diffusion model, the Boyd model, was employed to identify the rate-limiting step using eq 10:

$$B_t = -0.4977 - \ln(1 - F) \tag{10}$$

where F represents the fraction of MB adsorbed at any time t (min) and is calculated by eq 11:

$$F = \frac{q_t}{q_e} \tag{11}$$

Statistical Test. The nonlinear chi-square (χ^2) statistic test was performed in addition to the correlation coefficient (R) to discriminate the best model fit to the experimental data. A small χ^2 value demonstrates similarity between the modeled and experimental data, while a larger χ^2 demonstrates disparity. χ^2 was calculated using eq 12:

$$\chi^2 = \Sigma \frac{(q_e - q_{ecal})^2}{q_{ecal}} \tag{12}$$

where q_e is the experimental equilibrium adsorption capacity and $q_{e,cal}$ is the model equilibrium adsorption capacity.

Characterization Techniques. X-ray diffraction (XRD) analysis was conducted by using a Bruker D2 PHASER-e diffractometer using Cu-Kα radiation (0.15418 nm). Scanning electron microscopy (SEM) and energy-dispersive X-ray spectroscopy (EDX) were carried out on a cross-beam 540 FEG SEM microscope from Zeiss. UV−vis absorption measurements were conducted on a CARY 100 BIO UV−vis spectrophotometer. Fourier transform infrared spectroscopy (FTIR) spectroscopy was done on a Brunker Alpha Fourier transform spectrometer with platinum attenuated total reflectance sampling accessory. Thermal gravimetric analysis

(TGA) was done using an SDT Q600 V20.9 Build 20 Module DSC-TGA Standard. N_2 absorption/desorption isotherms were acquired using autosorb iQ model:7, ASiQWin version 5.2× at −196 °C, operating within a relative pressure (P/P_o) range of 0−1.0. Prior to measurement, the samples were predegassed at 130 °C for 18 h under vacuum. The Brunauer−Emmett−Teller (BET) and Barrett−Joyner−Halenda models were utilized to determine surface area and pore volume. X-ray photoelectron spectroscopy (XPS) was conducted on a Thermo model: ESCAlab 250Xi using a monochromatic Al Kα X-ray source.

■ RESULTS AND DISCUSSION

Material Characterization. *XRD.* Figure 1a illustrates the reference XRD pattern of MOF-5; Figure 1b shows the XRD
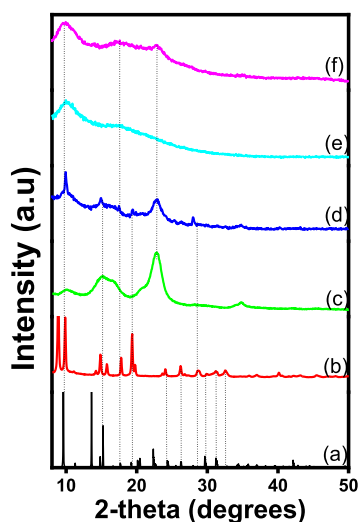
Figure 1. XRD patterns of (a) reference MOF-5, (b) MOF-5, (c) CNC, (d) MOF-5/CNC, (e) CA, and (f) CA-supported MOF-5/CNC.

pattern of the synthesized MOF-5 with peaks matching the reference XRD. The synthesized MOF-5 pattern is also consistent with the previously reported MOF-5 diffraction pattern.[43] The diffraction pattern exhibits peaks at 2-theta = ~8.5°, 9.9°, 14.9°, 15.8°, 17.8°, and 19.3°, which are characteristic of MOF-5 confirming successful synthesis of the material.[43−45] The crystallite size of MOF-5 was calculated using the Scherrer equation, shown in eq 13:

$$D = \frac{K\lambda}{\beta\cos\theta} \tag{13}$$

where D is the crystallite size, K is the Scherrer constant with a value of 0.9, β is the full width at half-maximum, and θ is the peak position. The size was calculated using peaks at 2θ positions 9.9°, 14.9°, 17.8°, and 19.3° and an average of 30.82 nm was considered the crystalline size of MOF-5.

Figure 1c shows the XRD pattern of CNC. This XRD pattern was observed to be consistent with previous reports and in line with JCPDC file no. 03-0226.[46,47] The diffraction pattern exhibited peaks at 2-theta = 15.2°, 16.7°, 22.6°, and 34.4°. These peaks are indexed as (110), (110), (200), and (004), respectively. Figure 1d depicts the MOF-5/CNC composite. This diffraction pattern exhibits a mixture of peaks from both the MOF-5 diffractogram and the CNC

diffractogram, which is desired, as it suggests that the two materials coexist within the composite. The figure displays peaks at 2-theta = 9.9°, 14.9°, and 28°, which belong to MOF-5; and the peaks at 15.2° and 22.6° belong to CNC. This observation suggests that the phase and the crystal structure of the individual materials are maintained during the formation of the composite. No new phases or crystal structures were observed when the two materials were combined. Figure 1e shows the XRD pattern of the highly amorphous CA material, with no well-defined peaks. The XRD pattern of the CA-supported MOF-5/CNC (Figure 1f) displayed broad peaks at 10° and 22.8°, which are characteristic of CA and the MOF-5/CNC nanocomposite.

FTIR. The synthesized materials were characterized by using FTIR spectroscopy. Figure 2a shows the CNC spectrum with
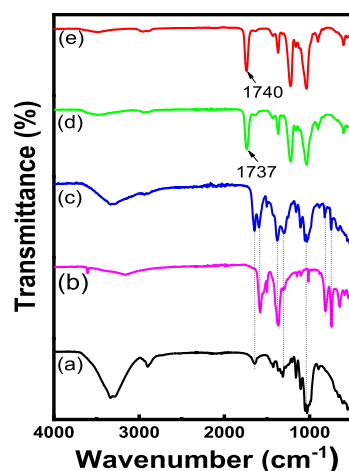

Figure 2. FTIR spectra of (a) CNC, (b) MOF-5, (c) MOF-5/CNC, (d) CA, and (e) CA-supported MOF-5/CNC.

functional group vibrations consistent with previous reports for CNC.[41,46,47] The peak at 1634 cm^{-1} is due to C=O stretching while the vibrations of the C−O−C pyranose ring are responsible for the peaks at 1430, 1374, and 1313 cm^{-1}. The peak observed at 892 cm^{-1} is because of glycosidic C$_1$−H deformation within the ring, which is characteristic of glycosidic linkages linking glucose monomers in the cellulose polymer. The FTIR spectra of MOF-5 (Figure 2b) show two peaks at 1381 and 1573 cm^{-1} due to asymmetric and symmetric stretching of carboxylate groups, respectively. The peak observed at 450 cm^{-1} is due to Zn−O stretching. The peaks observed at 743 and 815 cm^{-1} are due to C−H vibrations of the benzene ring. This FTIR spectrum coincides with MOF-5 spectra from previously reported studies confirming the successful synthesis of the material.[43,45] Figure 2c shows the spectrum of the MOF-5/CNC composite with peaks characteristic of CNC at 1648, 1310, and 1024 cm^{-1}. The peaks characteristic of MOF-5 are observed at 1583, 1364, 819, and 742 cm^{-1}. Figure 2d,e shows the FTIR spectra of CA and the adsorbent film, respectively. The peak at 1737 cm^{-1} in Figure 2d is due to carbonyl (C=O) stretching, and the peaks at 1028 and 1219 cm^{-1} are due to C−O−C symmetrical and asymmetrical vibrations, respectively. For the adsorbent film only peaks arising from CA are exhibited, this has been previously observed for CA nanocomposites.[42] The carbonyl (C=O) stretch in Figure 2e was shifted to 1740 cm^{-1}, indicating interaction between the MOF-5/CNC and the CA.
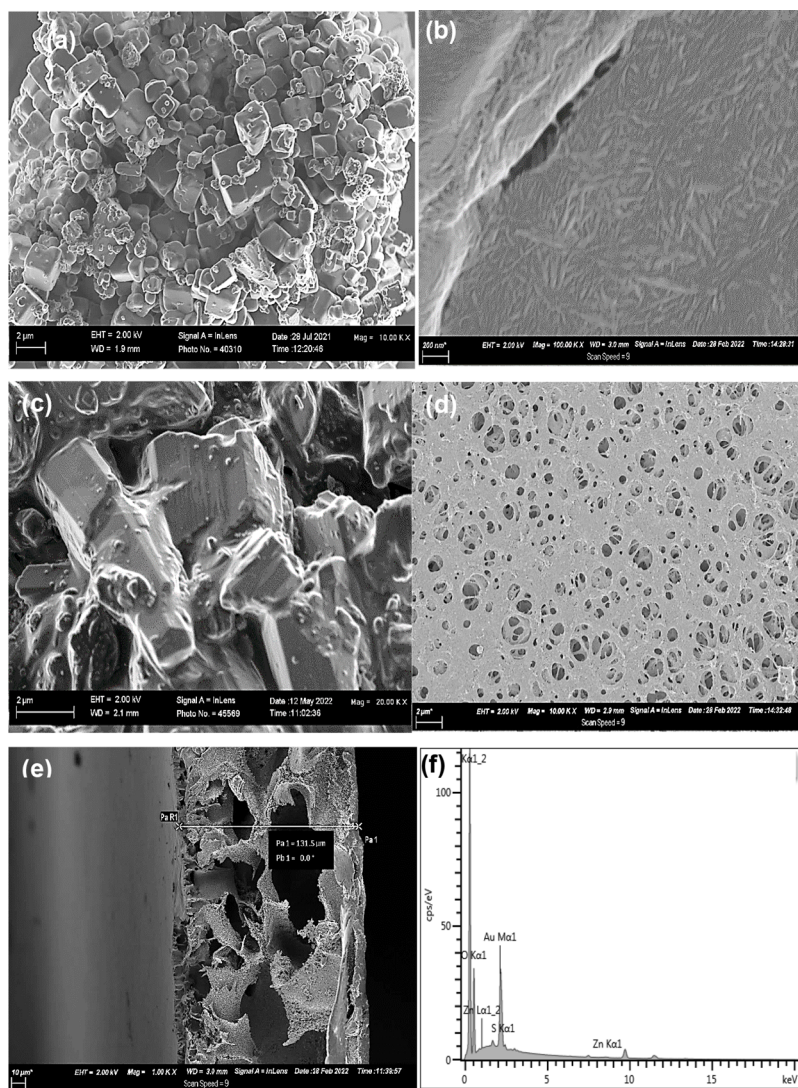
Figure 3. SEM images of (a) MOF-5, (b) CNC, (c) MOF-5/CNC, (d) CA-supported MOF-5/CNC film surface, (e) CA-supported MOF-5/CNC film cross-section, and (f) EDX spectrum of CA-supported MOF-5/CNC film.

SEM. The surface morphology of the materials was studied by using SEM. Figure 3a shows MOF-5 as mostly cubic crystals with particle sizes under 2 μm, consistent with previous reports.[40,43−45] The SEM image of CNC showed rod-like structures or nanowhiskers, which was the expected morphology.[46−48] The nanowhiskers have lengths of ca. 300 nm with diameters between 10 and 20 nm. The SEM image of MOF-5/CNC (Figure 3c) shows that the cubic crystals of MOF-5 were maintained; however, they appear to be coated with a thin layer of CNC. Figure 3d,e shows the SEM micrographs of the CA-supported MOF-5/CNC surface and cross-section, respectively. The surface of the adsorbent film is porous, and the adsorbent exhibits an irregular cross-section structure of dense skin layers and finger-like microcavities, which has been reported for CA-supported materials and membranes.[42,49] The film was synthesized via phase inversion, which results in a porous top layer and a finger-like sublayer. The film was measured to be 131.5 μm thick. Figure 3f shows the EDX spectrum of the film, and the elements observed, Zn and S, are from MOF-5 and CNC further confirming the successful synthesis of the adsorbent film.

TGA. TGA was used to assess the thermal stability of the adsorbent film. For all the materials (Figure 4a−d), the weight loss at 100 °C was attributed to loss of adsorbed water, and weight loss due to the removal of DMF occurred between 150 and 260 °C. The decomposition of the MOF-5 framework is
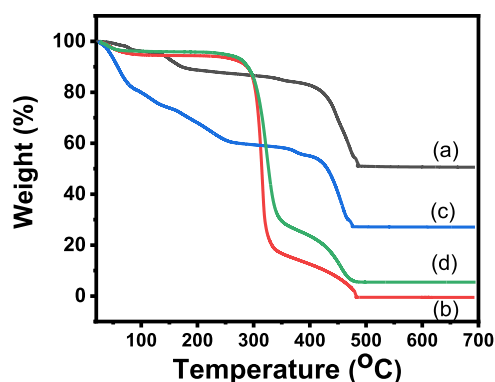

Figure 4. TGA curves of prepared (a) MOF-5, (b) CNC, (c) MOF-5/CNC, and (d) CA-supported MOF-5/CNC film.

shown in Figure 4a with weight loss in the range of 410−500 °C corresponding to the decomposition of the bridge between the Zn_4O carboxylate and the BDC ligand leaving a 51% zinc metal weight content. The CNC TGA curve shown in Figure 4b exhibits a second mass loss between 260 and 320 °C due to the pyrolysis of cellulose and hemicellulose. Further breakdown of the intermediates occurred beyond 340 °C until all the organic material was completely degraded. Figure 4c shows the weight loss of MOF-5/CNC. The weight loss between 410−500 °C is due to the decomposition of the composite, and 27% of zinc metal remains. The TGA curve of the CA-supported MOF-5/CNC film (Figure 4d) is slightly similar to the CNC curve since CA is a derivative of cellulose. Decomposition of the MOF-5 framework occurred between 360 and 500 °C, revealing a 5% zinc metal content.

BET and XPS. Figure 5 shows the N_2 adsorption−desorption isotherm of the adsorbent film. It can be observed that a type I
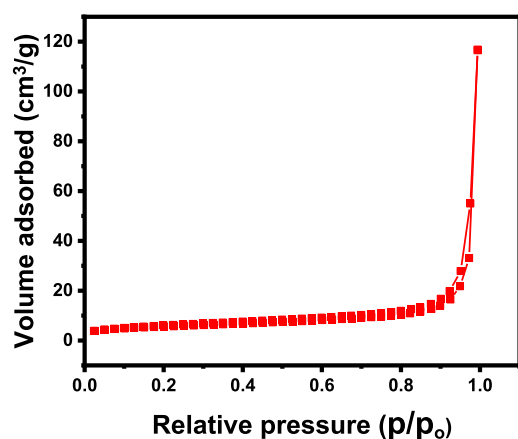

Figure 5. N_2 adsorption/desorption isotherm for the CA-supported MOF-5/CNC film.

adsorption−desorption isotherm was exhibited, and the specific surface area was determined to be 19.87 m^2/g. This renders the adsorbent microporous with a pore volume of 0.27 cm^3/g and a pore diameter of 1.17 nm. The elemental distribution of the adsorbent surface was studied by XPS. The presence of the O and C elements and their electronic state in the film are shown in Figure 6a. Figure 6b shows the deconvoluted carbon region depicting five peaks at 284.9, 284.2, 286.2, 286.2, and 287.5 eV assigned to sp^3-hybridized C−C, sp^2-hybridized C−C, C−O, and C═O bonds, respectively. The oxygen deconvoluted into two peaks at 531.9 and 532.9 eV (Figure 6c) assigned to C−O and C═O respectively.

Effect of pH on Adsorption of MB. The point of zero charge (pH_{pzc}) was used to determine the pH at which the net surface charge of the adsorbent film is zero. Figure 7 shows the plot of pH vs pH_i for the adsorbent and this study helps in understanding the surface chemistry involved during adsorption when the film interacts with MB. The figure shows the pH_{pzc} of the film to be 7.0. This means that the surface of the adsorbent film has a net positive charge in acidic pH and a net negative charge in alkaline pH.

Figure 8a shows the effect of pH on equilibrium adsorption capacity (q_e), and Figure 8b shows the effect of pH on % MB removal. pH has been observed to be a controlling parameter in the adsorption of MB.[50] The adsorption efficiency generally increases with increasing pH because, at an acidic pH, the

surface of the adsorbent is positively charged, resulting in electrostatic repulsions between the cationic adsorbent and the cationic MB, minimizing adsorption. In addition, at low pH, there are excess H^+ ions that compete with the cationic MB dye for adsorption sites making adsorption unfavorable. This is true at pH 5; however, there is an anomaly at pH 3. The error limit of pH 3 is within the error limit of pH 5, and as a result, the actual adsorption behavior is valid from pH 5 and above. At pH > pH_{pzc}, the negatively charged adsorbent is electrostatically attracted to the cationic MB, and this favors adsorption. This adsorbent is versatile, as it has the ability to adsorb cations or anions depending on the application. In this study, the analyte of interest is cationic, and the highest adsorption efficiency was observed at pH 11.

Effect of Contact Time on MB Adsorption. The optimized contact time was determined at optimum pH and at initial concentrations (1−6 mg/L). Figure 9 shows the effect of contact time on the adsorption capacity and percentage of MB removal. Adsorption occurred in three phases; the first hour was the initial phase, where adsorption took place at a relatively high rate as illustrated by the sharp increase in equilibrium adsorption capacity and percentage removal. Similar behavior has been observed for dyes on biosorbents.[51] This occurs because of the availability of vacant active sites on the adsorbent film. The second phase occurs when contact time increases to 4−5 h; at this stage, adsorption happens at a lower rate due to the gradual saturation of active sites on the surface of the adsorbent film, and adsorption equilibrium is reached after 5 h. The adsorption capacity at equilibrium was 4.29 mg/g, and this corresponds to a percentage removal of 77.4%.

Effect of Initial Concentration on MB Adsorption. The dependence of equilibrium adsorption capacity and % MB removal on initial MB concentration was studied at pH 11, contact time of 6 h, at 25 °C. Figure 10a shows the equilibrium adsorption capacity increases (q_e) linearly with initial concentration from 0.75 to 4.29 mg/g, while the % MB removal (Figure 10b) decreases in a parabolic fashion from 75 to 71.6%. The increasing MB adsorption at higher initial concentrations was influenced by mass transfer, these conditions result in the saturation of active sites causing a reduction in % MB removal. From these results, the initial concentration of 6 mg/L was considered as the optimal concentration.

Effect of Temperature on MB Adsorption. The influence of temperature on q_e and % MB removal was investigated under the optimized conditions, which include the initial concentration of 6 mg/L. When the temperature was increased from 25 to 45 °C equilibrium adsorption efficiency decreased from 4.29 to 3.02 mg/g (Figure 11a) and the % MB removal dropped from 71 to 51% (Figure 11b). The results show that MB interacts less with the adsorbent film as the temperature increases. This decrease in activity implies that the adsorption process was exothermic in nature.

Adsorption Isotherms. Langmuir's and Freundlich's adsorption isotherm models were used to determine the adsorption parameters for the adsorption process. Figure 12 illustrates the linear plots, and Table 1 lists the resulting parameters along with correlation coefficients (R^2) and nonlinear chi-square (χ^2) values. This study provides insight into the adsorbate and adsorbent surface interaction during the adsorption process. The Langmuir isotherm model, shown in Figure 12a, assumes the surface of the adsorbent is
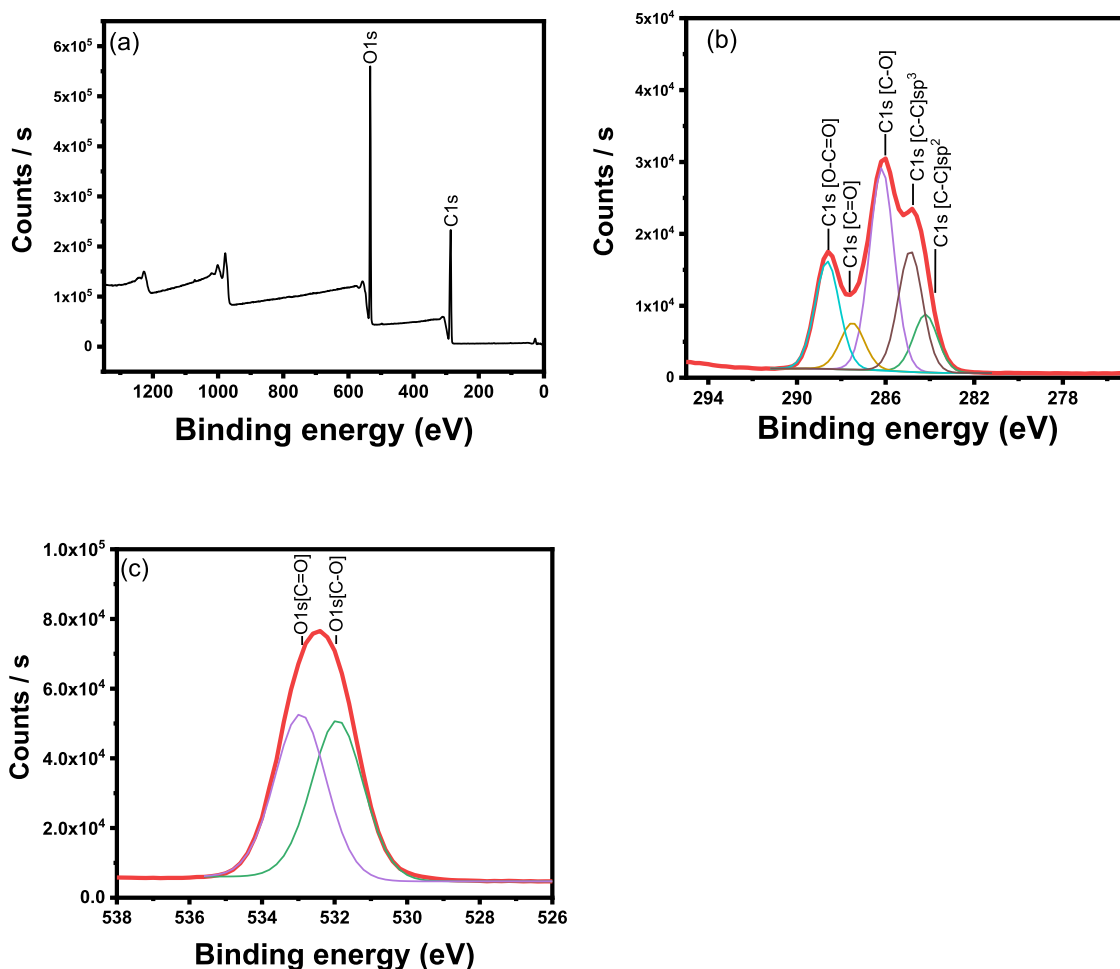
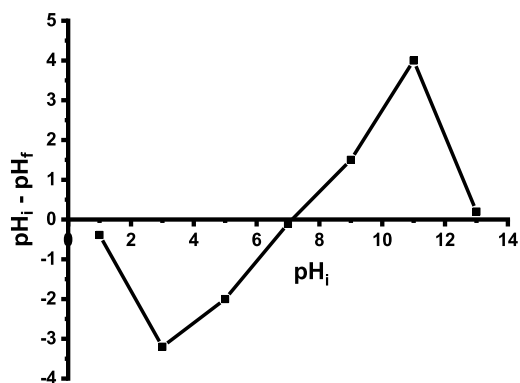**Figure 6.** (a) XPS survey and (b) C 1 s and (c) O 1 s spectra of the CA-supported MOF-5/CNC adsorbent film.

Figure 7. Plot of ΔpH vs pH$_i$.

homogeneous, and the maximum adsorption process occurs when monolayer coverage is achieved.[51] From Table 1, the R^2 value of the isotherm was 0.9738 and the χ^2 value was 0.011. The Langmuir constant, K_L, is dimensionless and represents the affinity of the adsorbent for the adsorbate. The K_L value in this study was 0.25, which is relatively high, suggesting that the interaction between the adsorbate and the adsorbent's surface is strong, implying that the adsorption process is favorable. The maximum adsorption capacity, q_{max} was calculated to be 13.23 mg/g and the separation factors, R_L, for all the initial concentration values, as illustrated by Figure 12c, was between 0 and 1 indicating a favorable adsorption process. The

Langmuir model showed a decent fit of the experimental data; however, the maximum monolayer capacity over-estimated (13.23 mg/g) the experimentally determined equilibrium capacity value of 4.29 mg/g. The Freundlich isotherm model assumes adsorption occurs on heterogeneous active sites with varying surface energies while following a multilayer coverage (Figure 12b). The R^2 value of the isotherm was 0.9674, and the χ^2 value was 0.031. From this curve, the heterogeneity factor, $1/n$, was between 0 and 1, indicating favorable adsorption. The Freundlich constant K_F was determined to be 2.77, and the equilibrium solid phase concentration was calculated using eq 14 to be 4.39 mg/g, which was closer to the experimental value (4.29 mg/g):

$$q_e = K_F C^{1/n} \tag{14}$$

The Freundlich constant presented a higher value compared to that of the Langmuir constant; this suggests that the adsorption mechanism may be described by the Freundlich isotherm. This indicates that the adsorption of MB on CA-supported MOF-5/CNC may conform to a mechanism involving multilayer coverage on a heterogeneous surface. Similar results have been observed on cellulose-based adsorbents for MB removal, showing better fitting with Freundlich isotherm.[52−54]

Adsorption Kinetic Models. Kinetic studies were used to investigate the potential rate-controlling step, as well as the adsorption mechanism. The adsorption kinetics are governed,
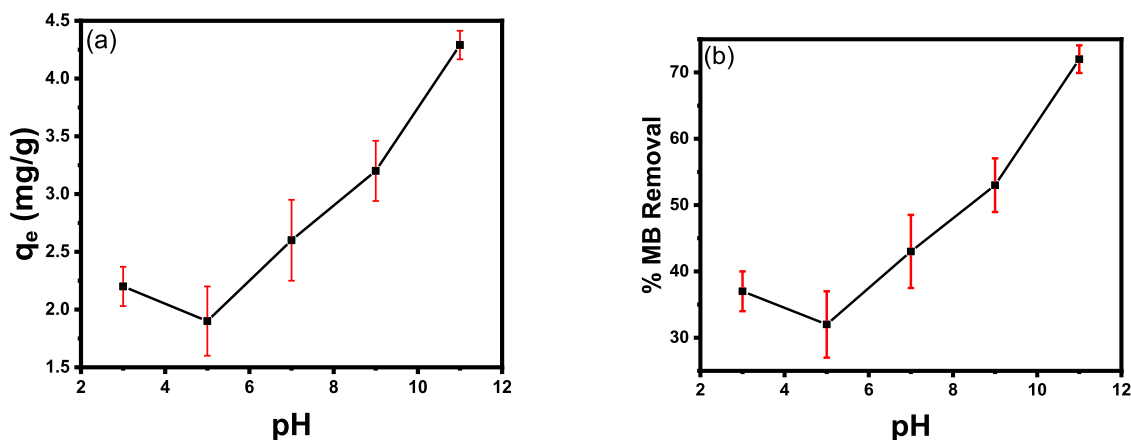
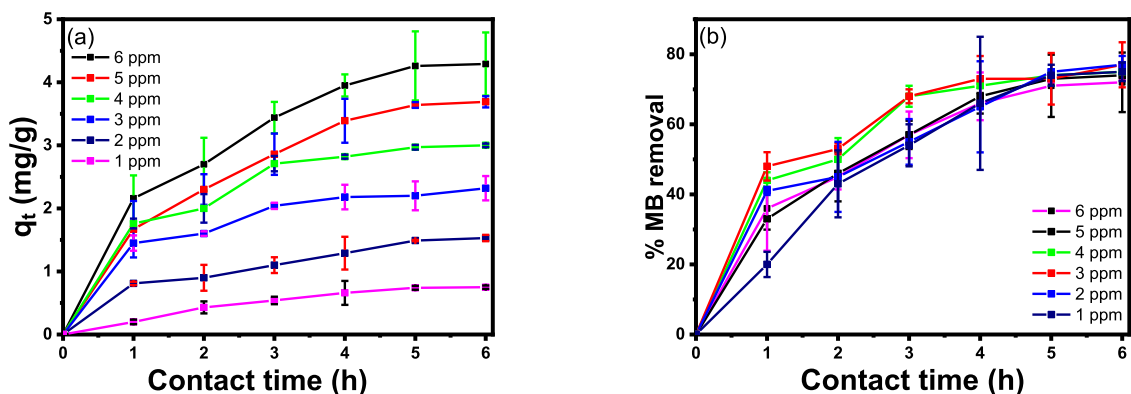**Figure 8.** (a) Equilibrium adsorption capacity vs pH, and (b) % MB removal vs pH.

Figure 9. (a) Effect of contact time on adsorption capacity at initial concentrations of 1−6 mg/L, and (b) effect of contact time on percentage MB removal at initial concentrations of 1−6 mg/L.
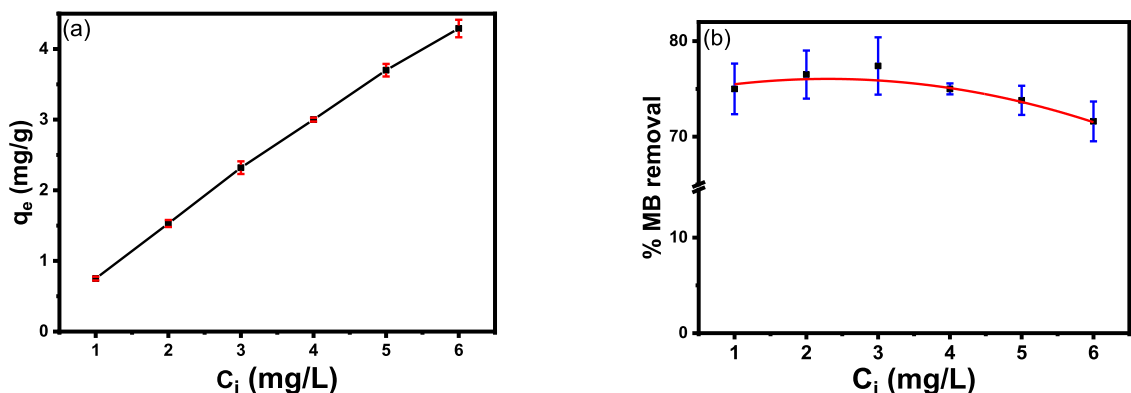

Figure 10. Plots of (a) equilibrium adsorption capacity vs initial concentration and (b) % MB removal vs initial concentration.

among various steps, by reaction processes and diffusion.[55] The adsorption data were fitted to the linearized pseudo-first-order kinetic model, and Figure 13a shows it was not applicable over the whole contact time and the calculated q_e was determined to be 13.21 mg/g. In most cases, the first order applies to the initial phase of the adsorption process and not to the rest of the contact time.[50,56] Figure 13b shows the experimental data fitting favorably over the whole adsorption range for the pseudo-second-order kinetic model. The calculated q_e from the pseudo-second-order model was determined to be 5.65 mg/g, which was closer to the experimentally obtained q_e (4.29 mg/g). The adsorption reaction can be described by pseudo-second-order kinetics

with chemical interactions dominating the adsorption process.[57,58] The kinetic parameters and corresponding R^2 and χ^2 values are listed in Table 1. Adsorption can proceed through various pathways, including external diffusion, intraparticle diffusion, and pore diffusion.[58] The intraparticle and/or pore diffusion typically influence the overall rate of the adsorption process. Figure 13c−e shows the fitting of experimental data for the diffusion models. The Weber−Morris plot (q_t vs $t^{1/2}$) in Figure 13c shows that the plot is linear with $R^2 > 0.9$ and $\chi^2 < 0.05$, indicating that intraparticle diffusion is a possible pathway for MB adsorption. For this model the linear fit has to pass through the origin; this suggests that intraparticle diffusion is not the only controlling mechanism in this
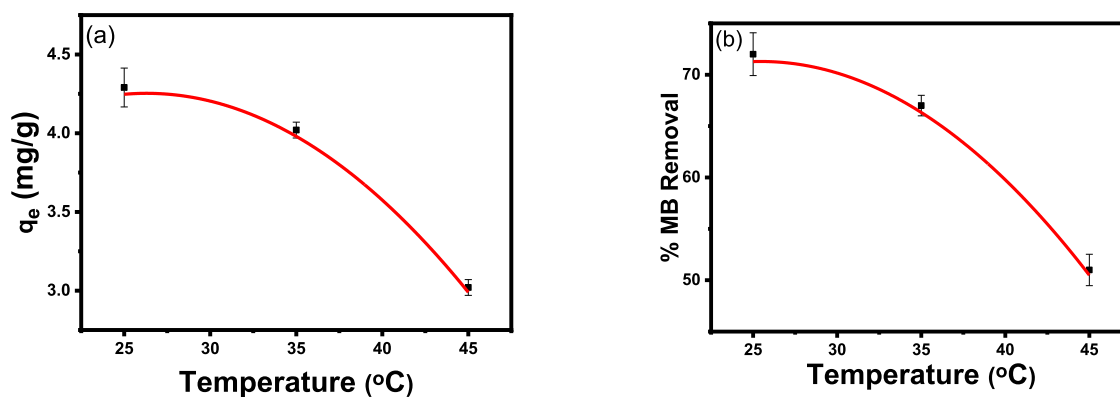
Figure 11. Effect of temperature on (a) equilibrium adsorption capacity and (b) % MB removal.
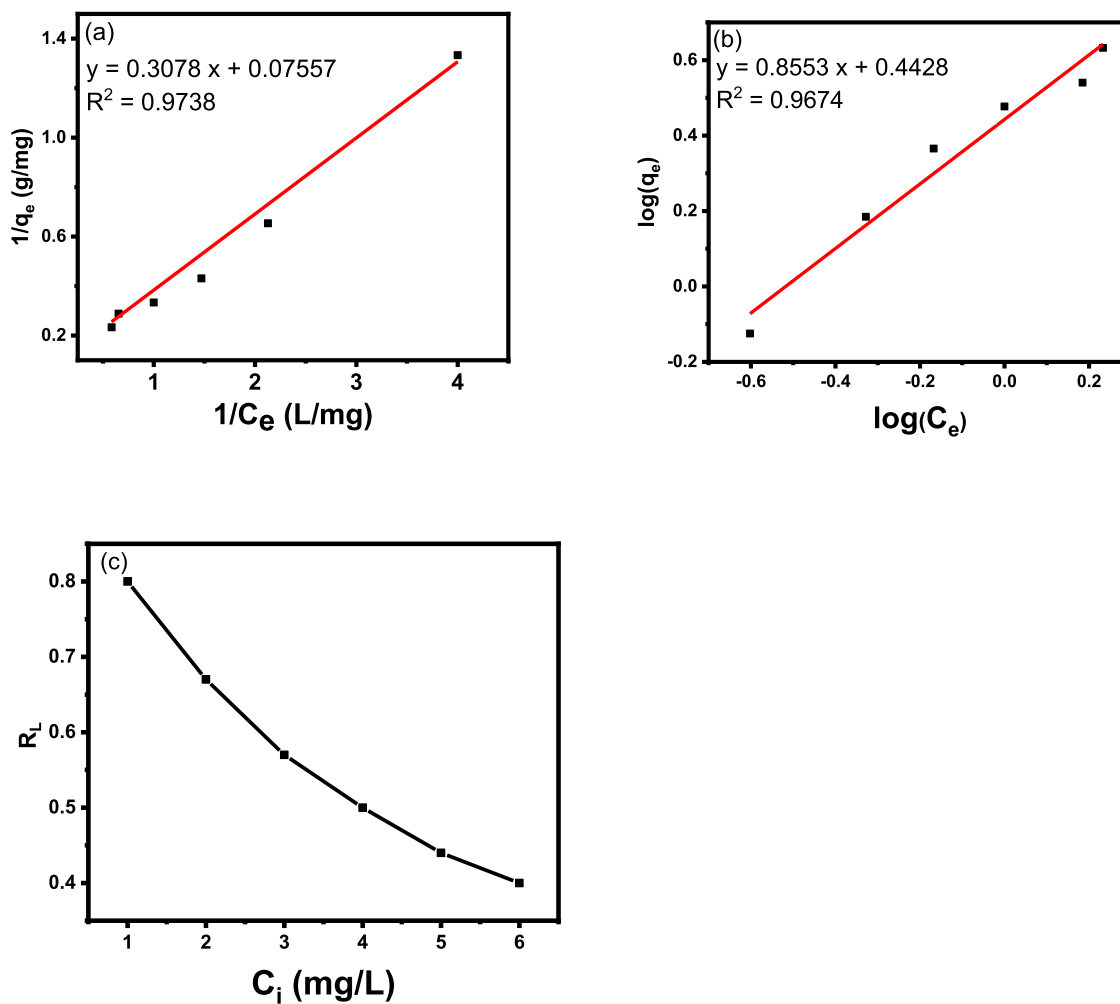

Figure 12. (a) Langmuir and (b) Freundlich isotherms of MB adsorption onto CA-supported MOF-5/CNC, and (c) R_L values from the Langmuir isotherm.

Table 1. Parameters for MB Adsorption on a CA-Supported MOF-5/CNC Film

| Langmuir	Freundlich	pseudo-first-order	pseudo-second-order	intraparticle diffusion model	Bangham model	pore diffusion
q_{max} (mg/g) 13.23	q_e (mg/g) 4.39	q_e (mg/g) 13.21	q_e (mg/g) 5.65	k_{id} 0.2073	K_B 0.098	1st segment slope 0.008
						2nd segment slope 0.04
K_L (L/mg) 0.25	K_F (mg/g) 2.77	k_1 0.00005	k_2 0.0021			1st intercept −0.31
R^2 0.9738	R^2 0.9674	R^2 0.9201	R^2 0.9864	R^2 0.9709	R^2 0.9726	2nd intercept −7.67
X^2 0.011	X^2 0.031	X^2 0.036	X^2 0.023	X^2 0.028	X^2 0.044	
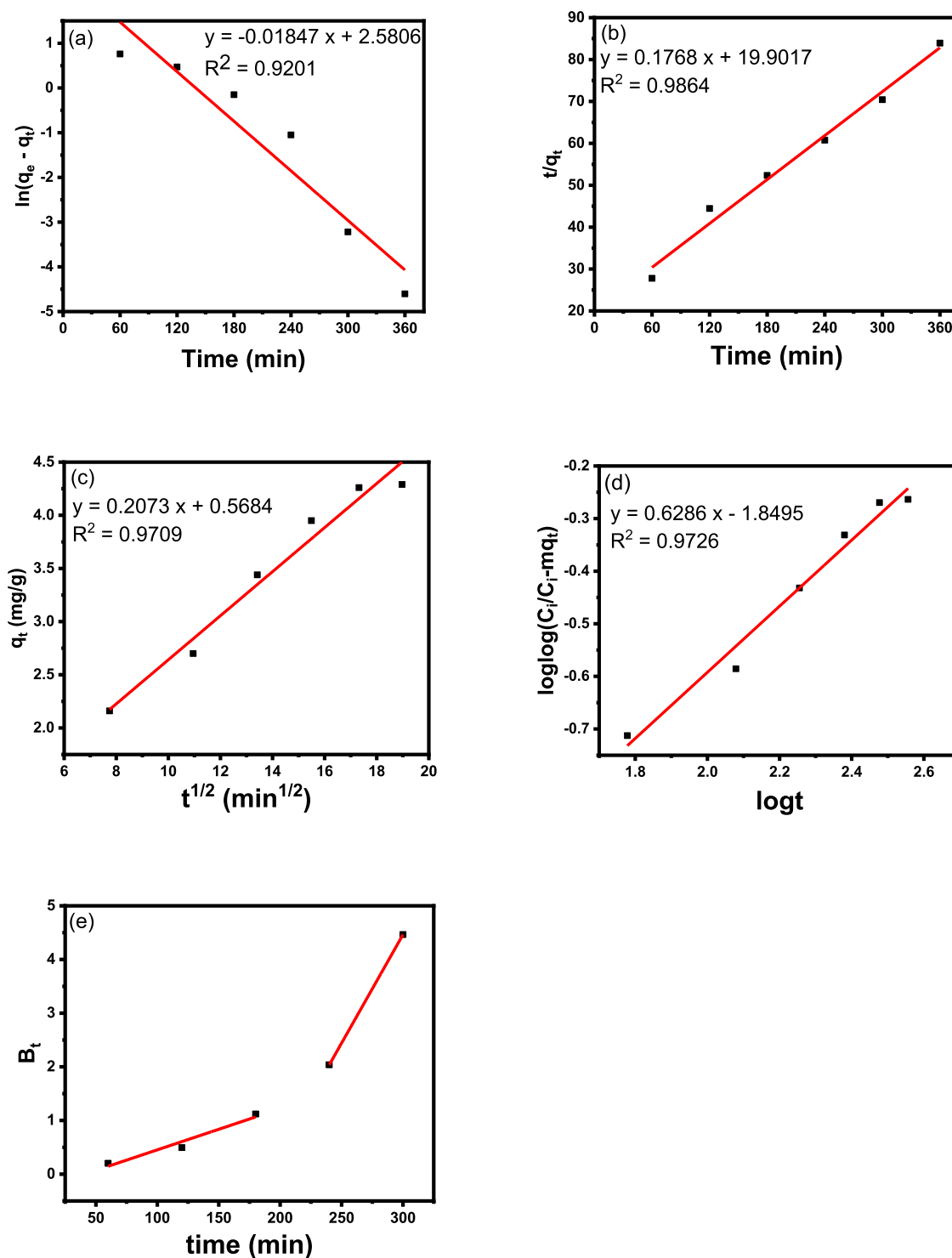
Figure 13. (a) Pseudo-first-order, (b) pseudo-second-order, (c) intraparticle, (d) pore diffusion, and (e) Boyd model plots of the experimental data for MB adsorption on the CA-supported MOF-5/CNC adsorbent film.

adsorption study but that the adsorption is a combination of multiple adsorption processes.[55,58] The intercept of the Weber−Morris plot has been reported to serve as an indicator of the thickness of the boundary layer, i.e., a large intercept implies a large boundary layer.[55,59] The Bangham plot shown in Figure 13d was used to check the possibility of pore diffusion as the rate-limiting step. The plot was found to be linear with $R^2 > 0.9$ and $\chi^2 < 0.05$, implying pore diffusion governs the adsorption process. The Boyd plot (Figure 13e)

was used to assess pore diffusion, and it shows multilinearity. The multilinearity represents succeeding adsorption processes.[57] Figure 13e can be described as two segments, the first between 60 and 180 min with an intercept close to zero; this indicates that adsorption in this period could be described by pore diffusion. In the second segment, the intercept suggests that other mechanisms described above have taken over the adsorption process.

Adsorption Thermodynamics. The Arrhenius equation, eq 15, was used to gain more insight into the type of adsorption:

$$\ln k = \ln A - \frac{E_a}{RT} \tag{15}$$

where k is the rate constant, A is the Arrhenius factor, E_a is the activation energy for the adsorption process, R is the gas constant (8.314 J/K.mol), and T is the temperature in Kelvin. The activation energies for physisorption are categorized between 5 and 40 kJ/mol and are between 40 and 800 kJ/mol for chemisorption.[60] The slope of Figure 14 was used to
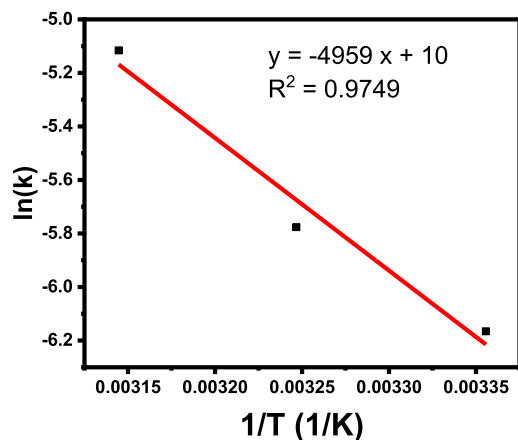

Figure 14. Plot of $\ln k$ vs T^{-1}: for the estimation of activation energy, E_a.

determine E_a, which was found to be 41.2 kJ/mol for the adsorption of MB on the adsorbent film, indicating chemisorption. Similar values have been observed for cellulose composites used for dye adsorption.[61]

Thermodynamic parameters which include standard entropy $(\Delta S°)$, standard enthalpy $(\Delta H°)$, and standard free energy $(\Delta G°)$ were determined to assess the thermal nature of MB adsorption on the adsorbent film according to previous reports.[51,57] $\Delta S°$ and $\Delta H°$ were calculated from the van't Hoff plot as depicted in Figure 15 according to eq 16:

$$\ln K_L = \frac{\Delta S°}{R} - \frac{\Delta H°}{RT} \tag{16}$$

$\Delta G°$ was determined using eq 17:

$$\Delta G° = -RT \ln K_L \tag{17}$$

Table 2 shows thermodynamic parameters derived from Figure 15. The $\Delta G°$ values became less negative with increasing temperature, indicating the occurrence of saturation on the adsorbent surface at increased temperatures; however, the process was thermodynamically spontaneous at higher temperatures. Furthermore, $\Delta S°$ was negative, and $\Delta H°$ was negative, signifying an exothermic adsorption process.

Proposed Adsorption Mechanism and Reusability Studies. The interaction of MB molecules with CA-supported MOF-5/CNC can be understood by using Figure 16. The presence of functional groups on the adsorbent film guarantees intermolecular interactions with dye molecules. The proposed adsorption mechanism of MB on the surface of the adsorbent occurs through several ways. FTIR showed the presence of hydroxyl and carbonyl groups on the adsorbent film. These
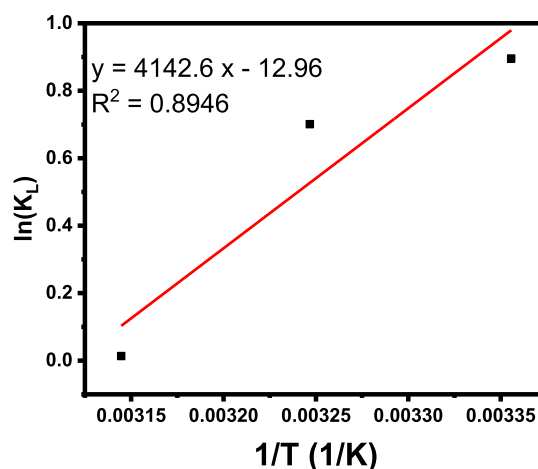

Figure 15. van't Hoff plot for MB adsorption on the CA-supported MOF-5/CNC adsorbent film.

Table 2. Thermodynamic Parameters for MB Adsorption on the CA-Supported MOF-5/CNC Adsorbent Film

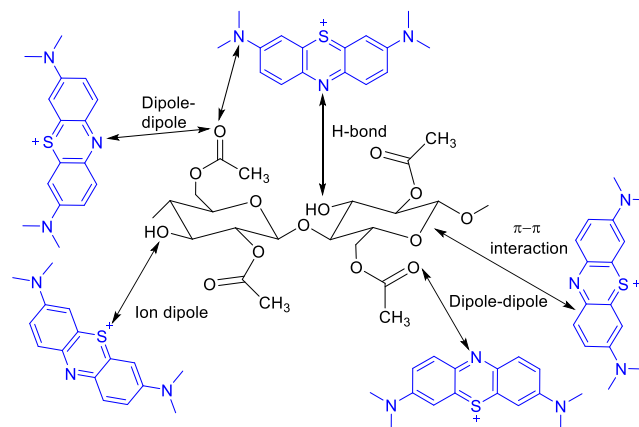| T/K	$\Delta G°$ (kJ/mol)	$\Delta H°$ (kJ/mol)	$\Delta S°$ (J/K.mol^{-1})	activation energy (E_a) (kJ/mol)
298	−2.21838	−34.44158	−107.749	41.2
308	−1.05112			
318	−0.03525			

Figure 16. Adsorption mechanisms of CA-supported MOF-5/CNC to MB.

groups can interact electrostatically with MB.[62] The interactions include ion-dipole forces, dipole−dipole, hydrogen bonding, and $\pi−\pi$ interactions, similar mechanisms have been proposed in the literature for MB adsorption.[63] During adsorption, since pH > pH_{pzc}, the negatively charged adsorbent is electrostatically attracted to the cationic MB, and this favors adsorption. In addition, the hydrogen atom from the hydroxyl groups can form hydrogen bonds with the nitrogen from MB as illustrated in Figure 16. $\pi−\pi$ interactions can also occur between the cellulose polymer chain and the MB aromatic ring.[64]

Adsorption efficiency was evaluated, as seen in Figure 17. Cycle 1 represents MB adsorption with a fresh adsorbent and cycles 2−5 represents the times the adsorbent has been desorbed in methanol and readsorbed in fresh MB solution. A 7% drop in the adsorption capacity was observed from cycle 1 to cycle 2. A 13% decrease in adsorption capacity was observed
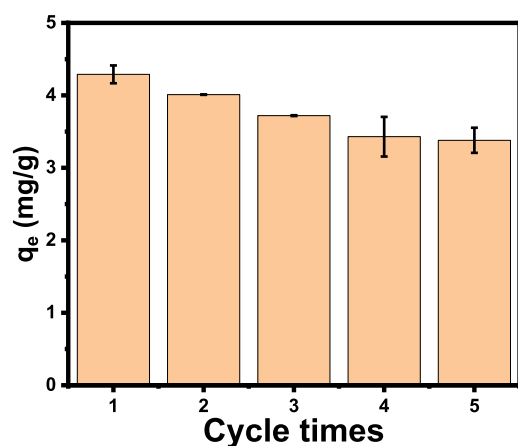
Figure 17. MB uptake over five adsorption/desorption cycles on CA-supported MOF-5/CNC.

for cycle 3 followed by a 20% decrease for cycle 4. These results support the thermodynamic data that allude to MB adsorption being driven by chemisorption resulting in reduced removal efficiency. There was no significant decrease after the fourth cycle (21% decrease for cycle 5), suggesting the binding sites were relatively fixed after the fourth cycle.

Simultaneous Adsorption of Methylene Blue and Methyl Orange (MO) and Treatment of Dye-Containing Wastewater. Dye-containing wastewater constitutes a complicated mixture of dyes, which include neutral, cationic, and anionic dyes. The simultaneous adsorption of anionic and cationic dyes is important for remediation hence the CA-supported MOF-5/CNC film was evaluated for the simultaneous adsorption for MB and MO at varied pH. As shown in Figure 18, MO had better adsorption under acidic conditions
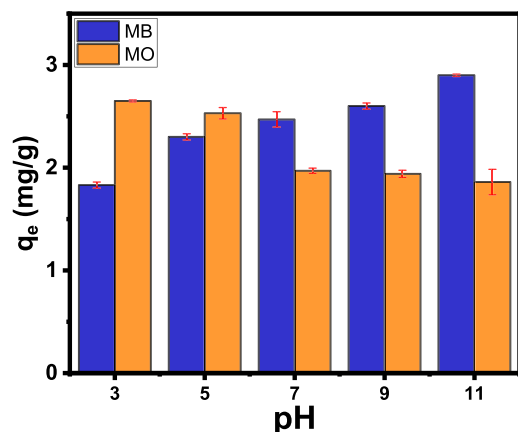

Figure 18. Simultaneous adsorption of MB and MO on the CA-supported MOF-5/CNC adsorbent film.

with the highest adsorption capacity of 2.65 mg/g obtained at pH 3. pH 11 remained the optimum pH for MB adsorption for the adsorbent film with an adsorption capacity of 2.9 mg/g, and MO had an adsorption capacity of 1.86 mg/g at this pH. The MB q_e values were lower than those reported without MO, this shows the influence of competing species for active sites.

The efficiency of the adsorbent film for wastewater treatment was examined by using domestic-industrial effluent spiked with MB. The pH of the wastewater sample was

determined to be 8.35. Figure 19 shows a decrease in the absorption spectra for MB post adsorption. The % removal of
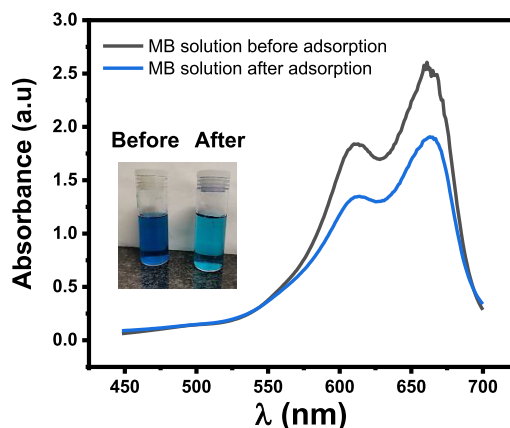

Figure 19. Adsorption of MB in domestic-industry effluent spiked with MB.

MB in the real water sample was determined to be 42%. The reduced efficiency was due to other contaminants interfering with the adsorption process.

Economic Assessment. In the development of any technological method applied in wastewater treatment, it is important to provide information about the cost of the treatment process. Depending on the treatment method, cost analysis is generally done by considering the costs of energy and material as major cost items.[65] For a material for which the purpose of the study is to investigate its efficiency in the removal of a dye, the simplified approach used in this study is considered sufficient.

In calculating the operating cost (OC), eq 18 was used:

$$OC\left(\frac{USD}{m^3}\right) = aC_{energy} + bC_{chemicals} \tag{18}$$

where C_{energy} and $C_{chemicals}$ are the energy consumed (in kWh/m^3) and the chemical consumption (in kg/m^3), respectively. The letter a is the electrical energy price USD 0.105 kWh for the South African market as of March 2024, and the letter b is the price of the chemicals used in the preparation of the adsorbent film material (USD/kg or USD/m^3).

In this study, the synthesized material could treat 0.030 L of wastewater in the first cycle; however, the calculated operating cost was done on the basis of treating 1 m^3 of the synthesized aqueous solution containing methylene blue following a reported approach.[66] The study considered the power rating in watts for all of the equipment used and the duration for which it was operated as well as the cost of the chemicals. Therefore, the total energy consumption was 110.8 kWh/m^3, which equates to USD 11.67/m^3, and the total chemical cost was USD 31.93/m^3. The operating cost was calculated to be USD 43.60. The operating cost for $C_{chemicals}$ was 2.8 times more expensive than that of C_{energy}.

Comparison with Other Adsorbents. A comparison of the maximum adsorption capacities for MB adsorption of MOF-cellulose composite adsorbents is shown in Table 3. An adsorbent based on MOF-derived porous carbon (MOF-DPC) nanoparticles supported on CA had a q_e value of 41.36 mg/g at an initial MB concentration of 50 mg·L^{-1} at 65 °C.[42] A cellulose aerogel fabricated from CA and ZIF-8 had a q_e value

Table 3. MB Maximum Adsorption Capacity of MOF-Cellulose-Based Adsorbents

adsorbent	q_e (mg/g)	ref
CA/MOF-DPC	41.36	42
ZIF-8 (CA@ZIF-8)	90.18	67
C-BZ-1000	227	68
CA-supported MOF-5/CNC	4.29	this study

of 90.18 mg/g.[67] The MOF was grown in situ on the surface of the adsorbent. A q_e value of 227 mg/g was determined from nitrogen-doped carbon aerogels fabricated from the carbonization of bacterial cellulose@ZIF-8 composite aerogels.[68] While these adsorbents show better q_e values, the fabrication processes require extreme temperatures that may affect the overall cost-effectiveness of the adsorbent.

■ CONCLUSIONS

A CA-supported MOF-5/CNC adsorbent film was successfully fabricated by using solvothermal and ultrasonication methods for methylene blue adsorption in aqueous media. The film showed a porous morphology with a measured film thickness of 131.5 μm. The integration of CNC and MOF into the CA support was confirmed by FTIR, SEM-EDX, TGA, and XPS. The CNC provided the adsorbent with hydrolytic stability, while the CA support secured the MOF. Various factors that influence MB batch adsorption were assessed, and the maximum adsorption capacity and % removal were determined to be 4.29 mg/g and 77.4%, respectively, at 25 °C, at an initial concentration of 6 mg/L, at pH 11 and at 14.7 wt % MOF loading. The adsorption process was spontaneous and exothermic as indicated by negative ΔG^o and ΔH^o values. The Freundlich and pseudo-second-order models were the best-fit adsorption isotherm and kinetic models, respectively, and the activation energy was consistent with chemisorption. Electrostatic interactions, such as dipole−dipole, $\pi-\pi$ interactions, and hydrogen bonding, were proposed as chemical interactions between methylene blue and the film to influence adsorption. After being regenerated five times, the film maintained 79% activity, indicating its value for reusability. The cost analysis for the adsorption was established. There was a 42% removal of MB when the film was applied for the treatment of wastewater. Overall, this work established a simple synthetic route for a MOF adsorbent film for water remediation.

■ AUTHOR INFORMATION

Corresponding Author

Nolwazi Nombona − *Department of Chemistry, University of Pretoria, Pretoria 0002, South Africa;* ● orcid.org/0000-0002-9946-2568; Email: nolwazi.nombona@up.ac.za

Author

Lebogang Manamela − *Department of Chemistry, University of Pretoria, Pretoria 0002, South Africa*

Complete contact information is available at:
https://pubs.acs.org/10.1021/acsomega.4c01150

Author Contributions

L.M. designed the project with the guidance of N.N. L.M. prepared the manuscript and N.N. proofread and made the contributions and suggestions to the structure and contents of the manuscript.

■ REFERENCES

(1) Al-Tohamy, R.; Ali, S.-S.; Li, F.; Okasha, K.-M.; Mahmoud, Y.-A.-G.; Elsamahy, T.; Jiao, H.; Fu, Y.; Sun, J. A critical review on the treatment of dye-containing wastewater: Ecotoxicological and health concerns of textile dyes and possible remediation approaches for environmental safety. *Ecotoxicol. Environ. Saf.* **2022**, *231*, No. 113160.

(2) Shathy, R.-A.; Fahim, S.-A.; Sarker, M.; Quddus, S.; Moniruzzaman, M.; Masum, S.; Molla, A.-I. Natural Sunlight Driven Photocatalytic Removal of Toxic Textile Dyes in Water Using B-Doped ZnO/TiO2 Nanocomposites. *Catalysts* **2022**, *12*, 308.

(3) Moyo, S.; Makhanya, B.-P.; Zwane, P.-E. Use of bacterial isolates in the treatment of textile dye wastewater: A review. *Heliyon* **2022**, *8*, No. e09632.

(4) Oladoye, P.-O.; Bamigboye, M.-O.; Ogunbiyi, O.-D.; Akano, M.-T. Toxicity and decontamination strategies of Congo red dye. *Groundw. Sustain. Dev.* **2022**, *19*, No. 100844.

(5) Khan, I.; Saeed, K.; Zekker, I.; Zhang, B.; Hendi, A.-H.; Ahmad, A.; Ahmad, S.; Zada, N.; Ahmad, H.; Shah, L.-A.; Shah, T.; Khan, I. Review on Methylene Blue: Its Properties, Uses, Toxicity and Photodegradation. *Water* **2022**, *14*, 242.

(6) Miao, G.; Li, F.; Gao, Z.; Xu, T.; Miao, X.; Ren, G.; Song, Y.; Li, X.; Zhu, X. Ag/polydopamine-coated textile for enhanced liquid/liquid mixtures separation and dye removal. *IScience* **2022**, *25*, No. 104213.

(7) Olas, B.; Białecki, J.; Urbanska, K.; Brys, M. The Effects of Natural and Synthetic Blue Dyes on Human Health: A Review of Current Knowledge and Therapeutic Perspectives. *Adv. Nutr.* **2021**, *12*, 2301−2311.

(8) Sunil, K.; Sherugar, P.; Rao, S.; Lavanya, C.; Geetha, R.; Balakrishna, G. R.; Arthanareeswaran, G.; Padaki, M. Prolific approach for the removal of dyes by an effective interaction with polymer matrix using ultrafiltration membrane. *J. Environ. Chem. Eng.* **2021**, *9*, No. 106328.

(9) Ihaddaden, S.; Aberkane, D.; Boukerroui, A.; Robert, D. Removal of methylene blue (basic dye) by coagulation-flocculation with biomaterials (bentonite and Opuntia ficus indica). *J. Water Process Eng.* **2022**, *49*, No. 102952.

(10) Qazi, U.-Y.; Iftikhar, R.; Ikhlaq, A. Application of Fe-RGO for the removal of dyes by catalytic ozonation process. *Environ. Sci. Pollut. Res.* **2022**, *29*, 89485−89497.

(11) Fu, Q.; Shi, D.; Mo, C.; Lou, J.; Zhou, S.; Zha, L.; Wang, J.; Yan, W.; Luo, J. Adsorption behavior of methylene blue on regenerable composite Cu-BTC@AG. *J. Solid State Chem.* **2022**, *311*, No. 123100.

(12) Nimbalkar, M.-N.; Bhat, B.-R. Simultaneous adsorption of methylene blue and heavy metals from water using Zr-MOF having free carboxylic group. *J. Environ. Chem. Eng.* **2021**, *9*, No. 106216.

(13) Ngulube, R.; Pillay, L.; Nombona, N. Synthesis and characterization of electrospun composite nanofibers from Moringa oleifera biomass and metal oxide nanoparticles as potential adsorbents for the removal of lead ions. *Chem. Pap.* **2024**, *78*, 599−611.

(14) Rashid, R.; Shafiq, I.; Akhter, P.; Iqbal, M.-J.; Hussain, M. A state-of-the-art review on wastewater treatment techniques: the

effectiveness of adsorption method. *Environ. Sci. Pollut. Res.* **2021**, *28*, 9050−9066.

(15) El-Bery, H.-M.; Saleh, M.; El-Gendy, R.-A.; Saleh, M.-R.; Thabet, S.-M. High adsorption capacity of phenol and methylene blue using activated carbon derived from lignocellulosic agriculture wastes. *Sci. Rep.* **2022**, *12*, 5499.

(16) Ali, J.; Bakhsh, E.-M.; Hussain, N.; Bilal, M.; Akhtar, K.; Fagieh, T.-M.; Danish, E.-Y.; Asiri, A.-M.; Su, X.; Khan, S.-B. A new biosource for synthesis of activated carbon and its potential use for removal of methylene blue and eriochrome black T from aqueous solutions. *Ind. Crops Prod.* **2022**, *179*, No. 114676.

(17) Hamad, H.-N.; Idrus, S. Recent Developments in the Application of Bio-Waste-Derived Adsorbents for the Removal of Methylene Blue from Wastewater: A Review. *Polymers* **2022**, *14*, 783.

(18) Sharma, G.; Sharma, S.; Kumar, A.; Lai, C.-W.; Naushad, M.; Shehnaz; Iqbal, J.; Stadler, F.-J. Activated Carbon as Superadsorbent and Sustainable Material for Diverse Applications. *Adsorpt. Sci. Technol.* **2022**.

(19) Alves, A.-T.; Lasmar, D.-J.; de Andrade Miranda, I.-P.; da Silva Chaar, J.; dos Santos Reis, J. The Potential of Activated Carbon in the Treatment of Water for Human Consumption, a Study of the State of the Art and Its Techniques Used for Its Development. *Adv. Biosci. Biotechnol.* **2021**, *12*, 143−153.

(20) Mohamed, F.; Shaban, M.; Zaki, S.-K.; Abd-Elsamie, M.-S.; Sayed, R.; Zayed, M.; Khalid, N.; Saad, S.; Omar, S.; Ahmed, A.-M.; Gerges, A.; El-Mageed, H.-R.; Soliman, N.-K. Activated carbon derived from sugarcane and modified with natural zeolite for efficient adsorption of methylene blue dye: experimentally and theoretically approaches. *Sci. Rep.* **2022**.

(21) El Messaoudi, N.; El Khomri, M.; El Mouden, A.; Bouich, A.; Jada, A. Regeneration and reusability of non-conventional low-cost adsorbents to remove dyes from wastewaters in multiple consecutive adsorption−desorption cycles: a review. *Biomass Convers. Biorefin.* **2022**, *14*, 1−18.

(22) Duan, Y.; Li, L.; Shen, Z.; Cheng, J.; He, K. Engineering Metal-Organic-Framework (MOF)-Based Membranes for Gas and Liquid Separation. *Membranes* **2023**, *13*, 480.

(23) Naser, S.-A.-E.; Badmus, K.-O.; Khotseng, L. Synthesis, Properties, and Applications of Metal Organic Frameworks Supported on Graphene Oxide. *Coatings* **2023**, *13*, 1456.

(24) Zhang, S.; Wang, J.; Zhang, Y.; Ma, J.; Huang, L.; Yu, S.; Chen, L.; Song, G.; Qiu, M.; Wang, X. Applications of water-stable metal-organic frameworks in the removal of water pollutants: A review. *Environ. Pollut.* **2021**, *291*, No. 118076.

(25) Al-Hazmi, G.-A.-A.; El-Zahhar, A.-A.; El-Desouky, M.-G.; El-Bindary, M.-A.; El-Bindary, A.-A. Adsorption of industrial dye onto a zirconium metal-organic framework: synthesis, characterization, kinetics, thermodynamics, and DFT calculations. *J. Coord. Chem.* **2022**, *75*, 1203−1229.

(26) Wang, X.; Zang, M.; Yang, J.; Yang, J.; Duan, H. Efficient removal of dyes from water by zirconium-based metal-organic cages with varying functional groups. *J. Mol. Stuct.* **2023**, *1291*, No. 136018.

(27) Chen, P.; Wang, Y.; Zhuang, X.; Liu, H.; Liu, G.; Lv, W. Selective removal of heavy metals by Zr-based MOFs in wastewater: New acid and amino functionalization strategy. *J. Environ. Sci.* **2023**, *124*, 268−280.

(28) Flores-Cervantes, D.-X.; Medina-Montiel, C.; Ramirez-Corona, N.; Navarro-Amador, R. Zirconium Based MOFs and Their Potential Use in Water Remediation: Current Achievements and Possibilities. *Air Soil Water Res.* **2022**, *15*, 1−15.

(29) Xue, W.; Wang, J.; Huang, H.; Mei, D. Structural and Hydrolytic Stability of Coordinatively Unsaturated Metal−Organic Frameworks $M_3(BTC)_2$ (M = Cu, Co, Mn, Ni, and Zn): A Combined DFT and Experimental Study. *J. Phys. Chem. C* **2021**, *125*, 5832−5847.

(30) An, Y.; Lv, X.; Jiang, W.; Wang, L.; Shi, Y.; Hang, X.; Pang, H. The stability of MOFs in aqueous solutions—research progress and prospects. *Green Chem. Eng.* **2024**, *5*, 187.

(31) Mosca, L.-P.-L.; Gapan, A.-B.; Angeles, R.-A.; Lopez, E.-C.-R. Stability of Metal−Organic Frameworks: Recent Advances and Future Trends. *Eng. Proc.* **2023**, *56*, 146.

(32) Li, Z.; Wang, L.; Qin, L.; Lai, C.; Wang, Z.; Zhou, M.; Xiao, L.; Liu, X.; Zhang, M. Recent advances in the application of water-stable metal-organic frameworks: Adsorption and photocatalytic reduction of heavy metal in water. *Chemosphere* **2021**, *285*, No. 131432.

(33) Ding, M.; Jiang, H.-L. Improving Water Stability of MOFs by a General Surface Hydrophobic Polymerization. *CCS Chem.* **2021**, *2*, 2740−2748.

(34) Yang, S.; Karve, V.-V.; Justin, A.; Kochetygov, I.; Espín, J.; Asgari, M.; Trukhina, O.; Sun, D.-T.; Peng, L.; Queen, W.-L. Enhancing MOF performance through the introduction of polymer guests. *Coord. Chem. Rev.* **2021**, *427*, No. 213525.

(35) He, Y.; Wang, Y.; Shi, J.; Lu, X.; Liu, Q.; Liu, Y.; Zhu, T.; Wang, D.; Yang, Q. Incorporating metal−organic frameworks into substrates for environmental applications. *J. Chem. Eng.* **2022**, *446*, No. 136866.

(36) Yu, B.; Liu, Y.; Li, Z.; Liu, Y.; Rao, P.; Li, G. Durable substrates incorporated with MOFs: Recent advances in engineering strategies and water treatment applications. *J. Chem. Eng.* **2023**, *455*, No. 140840.

(37) Yu, S.; Pang, H.; Huang, S.; Tang, H.; Wang, S.; Qiu, M.; Chen, Z.; Yang, H.; Song, G.; Fu, D.; Hu, B.; Wang, X. Recent advances in metal-organic framework membranes for water treatment: A review. *Sci. Total Environ.* **2021**, *800*, No. 149662.

(38) Dehghankar, M.; HmtShirazi, R.; Mohammadi, T.; Tofighy, M.-A. Synthesis and modification methods of metal-organic frameworks and their application in modification of polymeric ultrafiltration membranes: A review. *J. Environ. Chem. Eng.* **2023**, *11*, No. 109954.

(39) Salahuddin, N.; Akelah, A.; Elnagar, M.; Abdelwahab, M.-A. Antibacterial and cytotoxicity of methylene blue loaded-cellulose nanocarrier on breast cancer cell line. *Carbohyd. Polym. Technol. Appl.* **2024**, *2*, No. 100138.

(40) Peedikakkal, A.-M.-P.; Aljundi, I.-H. Upgrading the Hydrogen Storage of MOF-5 by Post-Synthetic Exchange with Divalent Metal Ions. *Metal Ions. Appl. Sci.* **2021**, *11*, 11687.

(41) Matebie, B.-Y.; Tizazu, B.-Z.; Kadhem, A.-A.; Prabhu, S.-V. Synthesis of Cellulose Nanocrystals (CNCs) from Brewer's Spent Grain Using Acid Hydrolysis: Characterization and Optimization. *J. Nanomater.* **2021**, *2021*, 10.

(42) Tahazadeh, S.; Karimi, H.; Mohammadi, T.; Motejadded, H.-B.; Tofighy, M.-A. Fabrication of biodegradable cellulose acetate/MOF-derived porous carbon nanocomposite adsorbent for methylene blue removal from aqueous solutions. *J. Solid State Chem.* **2021**, *299*, No. 122180.

(43) Fiaz, M.; Kashif, M.; Fatima, M.; Batool, S.-R.; Asghar, M.-A.; Shakeel, M.; Athar, M. Synthesis of Efficient TMS@MOF-5 Catalysts for Oxygen Evolution Reaction. *Catal. Lett.* **2020**, *150*, 2648−2659.

(44) Asadevi, H.; Prasannakumaran, P.; Kumari, N.-C.; Amma, R.-P.; Khadar, S.-A.; Sasi, S.-C.; Raghunandan, R. ZnO@MOF-5 as a Fluorescence "Turn-Off" Sensor for Ultrasensitive Detection as well as Probing of Copper(II) Ions. *ACS Omega* **2022**, *7*, 13031−13041.

(45) Hu, Y.; Yang, H.; Wang, R.; Duan, M. Fabricating Ag@MOF-5 nanoplates by the template of MOF-5 and evaluating its antibacterial activity. *Colloids Surf. A: Physicochem. Eng.* **2021**, *626*, No. 127093.

(46) Imiete, I.-E.; Giannini, L.; Tadiello, L.; Orlandi, M.; Zoia, L. The effect of sulfate half-ester groups on the mechanical performance of cellulose nanocrystal-natural rubber composites. *Cellulose* **2023**, *30*, 8929−8940.

(47) Leong, S.-L.; Tiong, S.-I.-X.; Siva, S.-P.; Ahamed, F.; Chan, C.; Lee, C.-L.; Chew, I.-M.-L.; Ho, Y.-K. Morphological control of cellulose nanocrystals via sulfuric acid hydrolysis based on sustainability considerations: An overview of the governing factors and potential challenges. *J. Environ. Chem. Eng.* **2022**, *10*, No. 108145.

(48) Zhu, W.; Han, M.; Kim, D.; Zhang, Y.; Kwon, G.; You, J.; Jia, C.; Kim, J. Facile preparation of nanocellulose/Zn-MOF-based catalytic filter for water purification by oxidation process. *Environ. Res.* **2022**, *205*, No. 112417.

(49) Azam, R.-S.; Almasri, D.-A.; Alfahel, R.; Hawari, A.-H.; Hassan, M.-K.; Elzatahry, A.-A.; Khaled, A. MXene (Ti3C2Tx)/Cellulose Acetate Mixed-Matrix Membrane Enhances Fouling Resistance and Rejection in the Crossflow Filtration Process. *Membranes* **2022**, *12*, 406.

(50) Şendal, K.; Özgür, M.-U.; Gülen, J. Biosynthesis of ZnO photocatalyst and its application in photo catalytic degradation of methylene blue dyestuff. *J. Disper. Sci. Technol.* **2023**, *44*, 2734−2747.

(51) Gülen, J.; Gezerman, A.-O. A novel biosorbent for remediation of colored waste water. *Biomass Conv. Bioref.* **2023**, *13*, 3227−3235.

(52) Melese, H.; Tsade, H. Cellulose based adsorbent for cationic methylene blue dye removal. *Discovery Appl. Sci.* **2024**.

(53) Amrutha; Jeppu, G.; Girish, C.-R.; Baakrishna, P.; Mayer, K. Multi-component Adsorption Isotherms: Review and Modeling Studies. *Environ. Process* **2023**, *10*, 38.

(54) Khatri, M.; Ahmed, M.-E.; Al-Juboori, R.-A.; Khanzada, N.-K.; Hilal, N. Reusable environmentally friendly electrospun cellulose acetate/cellulose nanocrystals nanofibers for methylene blue removal. *J. Environ. Chem. Eng.* **2024**, *12*, No. 111788.

(55) Wang, J.; Guo, X. Rethinking of the intraparticle diffusion adsorption kinetics model: Interpretation, solving methods and applications. *Chemosphere* **2022**, *309*, No. 136732.

(56) Gülen, J.; Akın, B.; Özgür, M. Ultrasonic-assisted adsorption of methylene blue on sumac leaves. *Desalin. Water Treat.* **2016**, *57*, 9286.

(57) Gülen, J.; İskeçeli, M. Removal of methylene blue by using porous carbon adsorbent prepared from carbonized chestnut shell. *Materials Testing* **2017**, *59*, 188−194.

(58) Mekuria, D.; Diro, A.; Melak, F.; Asere, T.-G. Adsorptive Removal of Methylene Blue Dye Using Biowaste Materials: Barley Bran and Enset Midrib Leaf. *J. Chem.* **2022**, *2022*, 1.

(59) Gülen, J.; Zorbay, F. Methylene Blue Adsorption on a Low Cost Adsorbent—Carbonized Peanut Shell. *Water Environ. Res.* **2017**, *89*, 805.

(60) Alharby, N.-F.; Almutairi, R.-S.; Mohamed, N.-A. Adsorption behavior of methylene blue dye by novel cross-linked O-CM-Chitosan hydrogel in aqueous solution: kinetics, isotherm and thermodynamics. *Polymers* **2021**, *13*, 3659.

(61) Zaman, A.; Orasugh, J.-T.; Banerjee, P.; Dutta, S.; Ali, M.-S.; Das, D.; Bhattacharya, A.; Chattopadhyay, D. Facile one-pot in-situ synthesis of novel graphene oxide-cellulose nanocomposite for enhanced azo dye adsorption at optimized conditions. *Carbohydr. Polym.* **2020**, *246*, No. 116661.

(62) Wu, Z.; Liao, Q.; Chen, P.; Zhao, D.; Huo, J.; An, M.; Li, Y.; Wu, J.; Xu, Z.; Sun, B.; Huang, M. Synthesis, characterization, and methylene blue adsorption of multiple-responsive hydrogels loaded with Huangshui polysaccharides, polyvinyl alcohol, and sodium carboxyl methyl cellulose. *Int. J. Biol. Macromol.* **2022**, *215*, 157−171.

(63) Yang, T.; Li, Z.; Wei, W.; Wang, X.; Liu, F.; Xu, X.; Liu, Z. Structure and Properties of Lignin Extracted from Cotton Stalk by Non-polluting Ethanol-Assisted Hot Water Pretreatment and its High-Value Utilization for Methylene Blue Removal. *Waste Biomass Valor.* **2023**, *14*, 2085−2101.

(64) Rana, J.; Goindi, G.; Kaur, N.; Krishna, S.; Kakati, A. Synthesis and application of cellulose acetate-acrylic acid-acrylamide composite for removal of toxic methylene blue dye from aqueous solution. *J. Water Process Eng.* **2022**, *49*, No. 103102.

(65) Kobya, M.; Delipinar, S. Treatment of the baker's yeast wastewater by electrocoagulation. *J. Hazard. Mater.* **2008**, *154*, 1133−1140.

(66) Bayramoglu, M.; Kobya, M.; Can, O.-T.; Sozbir, M. Operating cost analysis of electrocoagulation of textile dye wastewater. *Sep. Purif. Technol.* **2004**, *37*, 117−125.

(67) Wu, G.; Zhou, C.; Li, H.; Xia, S.; Zhu, Y.; Han, J.; Xing, W. Controlled fabrication of the biomass cellulose aerogel@ZIF-8 nanocomposite as efficient and recyclable adsorbents for methylene blue removal. *Ind. Crop. Prod.* **2023**, *193*, No. 116169.

(68) Ma, X.; Xu, Y. Three-dimensional porous nitrogen-doped carbon aerogels derived from cellulose@mof for efficient removal of dye in water. *J. Environ. Chem. Eng.* **2022**, *10*, No. 108385.